

A Critical Analysis of Least-Squares Tensor Hypercontraction Applied to MP3

Devin A. Matthews^{1, a)}

Southern Methodist University, Dallas, TX 75275, USA

The least-squares tensor hypercontraction (LS-THC) approach is a promising method of reducing the high polynomial scaling of wavefunction methods, for example those based on many-body perturbation theory or coupled cluster. Here, we focus on LS-THC-MP3, and identify four variants with differing error and efficiency characteristics. The performance of LS-THC-MP3 is analyzed for regular test systems with up to 40 first-row atoms. We also analyze the size-extensivity/size-consistency and grid- and basis set-dependence of LS-THC-MP3. Overall, the errors observed are favorably small in comparison with standard density fitting, and a more streamlined method of generating grids via pruning is suggested. Practical crossover (the point at which LS-THC-MP3 is cheaper than the canonical method) is achieved around 240 correlated electrons. Despite several drawbacks of LS-THC that have been identified: a small but non-zero size-consistency error, poor description of angular correlation, and potentially large increase of error with basis set size, the results show that LS-THC has significant potential for practical application to MP3 and other wavefunction methods.

^{a)}Electronic mail: damatthews@smu.edu

I. INTRODUCTION

The problem of the steep polynomial scaling of the computational cost of quantum chemical methods, in particular those based on explicit wavefunction representations, is one of the major roadblocks in extending accurate computational methods to large and complex systems. It has long been known that electronic interactions (in neutral systems), including dynamical electron correlation, are inherently “near-sighted”.¹ This fact has led to the development of a number of localized electron correlation methods, including those based on pair natural orbitals,^{2–5} molecular fragmentation,^{6,7} Hilbert-space localization,^{8–11} atomic orbital representations,¹² and others. For total energies, such approaches have been very successful, and such techniques have even been extended to excited state energies and other properties,^{13–16} albeit with some limitations.

In another direction, there has been less vigorous research into the fact that electronic interactions are inherently structured. In this viewpoint, one considers a global representation of electronic interactions, either the two-electron Hamiltonian or the parameters of the wavefunction ansatz (e.g. cluster amplitudes), and attempts to discover approximate forms which reduce the dimensionality and scaling of the correlation problem. A simple example is given by the CANDECOMP/PARAFAC¹⁷ (CP—later backronymed to canonical polyadic¹⁸) decomposition applied to the two-electron part of the Hamiltonian, \hat{G} , expressed as a 4-dimensional tensor,

$$g_{\rho\sigma}^{\mu\nu} \equiv \langle \mu\nu | \hat{g} | \rho\sigma \rangle \approx \sum_{r=1}^R U_{\mu r} V_{\nu r} W_{\rho r} X_{\sigma r}$$

where permutational symmetry has not been imposed. Note that the non-antisymmetrized integrals are used here. Instead of a single 4-dimensional tensor, one only has to deal with four matrices, and assuming that the number of factors, R , grows linearly with molecular size, reduced scaling both in storage and in computation. While the CP decomposition provides a relatively simple example of tensor decompositions, and how they can lead to reduction in computational scaling,¹⁹ a practical and feasible implementation of CP for large molecules has not as yet been developed.

A somewhat more promising alternative is the tensor hypercontraction (THC) approach,²⁰ especially the least-squares (LS-THC) variant.²¹ The THC factorization is itself similar to but slightly more complex than the CP format, having now five matrix components, but the

real advantage of LS-THC is that four out of these five matrices can be trivially computed given a suitable set of real-space grid points. The remaining matrix can be determined in closed form by fitting the Hamiltonian (or wavefunction components). In contrast, determining the CP or direct THC decomposition is a highly non-linear process which is fraught with convergence problems.^{17,22,23} LS-THC, applied to the Hamiltonian, is exceptionally effective in accurately reproducing e.g. MP2 energies with rather small grids²⁴ (scaling linearly with system size, and with a number of points similar to or fewer than typical auxiliary basis sets used for density fitting). Largely, we can attribute this success to the fact that the bare Coulomb interaction is entirely local (in a different sense than for local correlation methods): an integral over the Coulomb operator can be exactly computed using a real-space quadrature over a grid. This same property is responsible for the favorable computational properties of local density functional methods as well as density fitting/resolution-of-the-identity approaches.

The wavefunction, however, is another story. Taking the doubles amplitudes from configuration interaction (CI) or, neglecting for a moment higher-order terms, from coupled cluster (CC), we can consider these as integrals over a “two-electron interaction kernel”,

$$c_{ij}^{ab} \sim t_{ij}^{ab} = \langle ab | \hat{\tau} | ij \rangle$$

At first order in Møller-Plesset perturbation theory, and we have,

$$(t^{[1]})_{ij}^{ab} = \frac{g_{ij}^{ab}}{\epsilon_i + \epsilon_j - \epsilon_a - \epsilon_b}$$

Numerical experiments confirm that these amplitudes have both linear (or at least sub-quadratic) CP rank²⁵ as well as linear SVD rank (formatted as an $ai \times bj$ matrix).²⁶ Initial applications of LS-THC to cluster amplitudes also support a low-rank structure,^{22,27} which are confirmed by results in this work. The CP rank of the orbital energy denominators is actually constant, as evidenced by the Laplace transform technique.²⁸ In total, the cluster amplitudes appear to be manifestly factorizable.

Nonetheless, an important difference remains: the two-electron interaction kernel is not a local operator. In this work, we demonstrate numerically that the LS-THC decomposition is inherently less accurate for double amplitudes, compared to Coulomb integrals. Additionally, we show that the form of LS-THC necessary for treating iterative methods like CCSD incurs additional errors due to forced approximation of exchange integrals. This is in sharp contrast

to the expectations of Hohenstein et al. that, “If more fidelity is required in the correlation energies, it is possible to simply use denser grids.”²⁷ While this statement seems reasonable given that the LS-THC decomposition does indeed become exact when $N(N+1)/2$ grid points are employed, we show that errors for practical grid sizes may be large and slowly decreasing. Despite this theoretical shortcoming of LS-THC, we do show that errors in MP3 energies when employing LS-THC-decomposed $\hat{T}_2^{[1]}$ or $\hat{T}_2^{[2]}$ amplitudes can be made quite reasonable. Most importantly, we show that our implementation of LS-THC-MP3 achieves practical crossover around 240 correlated electrons, a point which will steadily move towards smaller systems as grid size and implementation efficiency are improved.

II. THEORY

The LS-THC decomposition imposes a CP-like structure on the two-electron Hamiltonian elements,²⁰

$$g_{\rho\sigma}^{\mu\nu} \approx \sum_{RS=1}^{n_P} X_{\mu}^R X_{\rho}^R V_{RS} X_{\nu}^S X_{\sigma}^S$$

where n_P is the number of grid-points. We have used the standard notation for atomic orbital (AO) and molecular orbital (MO) indices, with $\mu\nu\rho\sigma$ denoting AOs, $abcdef$ denoting virtual MOs, and $ijklmn$ denoting occupied MOs. Capital Roman letters $RSTUVWXY$ will be used to denote grid points; it should be noted that we will also make use of \mathbf{T} , \mathbf{V} , and \mathbf{X} matrices, with elements such as T_{RS} , V_{UW} , X_{μ}^Y etc. (as above), and that these should not be confused with grid indices.

In this work, we use grid points pruned from an initial Becke-style²⁹ molecular grid using the Cholesky decomposition approach of Ref. 30. The collocation matrix \mathbf{X} is determined by simple evaluation of the orbitals at the grid points, weighted by the fourth root of the grid quadrature weights. The LS-THC decomposition also applies directly to integrals in the molecular orbital basis,

$$g_{rs}^{pq} \approx \sum_{R=1}^{n_{pr}} \sum_{S=1}^{n_{qs}} (X^{(pr)})_p^R (X^{(pr)})_r^R V_{RS}^{(pqrs)} (X^{(qs)})_q^S (X^{(qs)})_s^S$$

where now we may have one of three grids determining $\{\mathbf{X}^{(ab)}, \mathbf{X}^{(ai)}, \mathbf{X}^{(ij)}\}$ collocation matrices with $\{n_{ab}, n_{ai}, n_{ij}\}$ grid points, respectively. \mathbf{V} is determined uniquely for each of the $abcd$, $abci$, $abij$, $aibj$, $aijk$, and $ijkl$ MO distributions (note these are in Dirac order). These

indices on \mathbf{X} , \mathbf{V} , and n only convey the relevant MO distributions (occupied/virtual) and are not indices in the usual sense. In each case, the “core” matrix \mathbf{V} is determined by a least-squares fit,²¹

$$V_{RS} = \sum_{TU=1}^{n_P} S_{RT}^{-1} X_\mu^T X_\rho^T g_{\rho\sigma}^{\mu\nu} X_\nu^U X_\sigma^U S_{US}^{-1}$$

with $S_{RS} = \sum_{\mu\nu} X_\mu^R X_\nu^R X_\mu^S X_\nu^S$, and S_{RS}^{-1} is an element of the matrix inverse of \mathbf{S} . We have used the AO integrals here for example; the procedure is the same for the MO integrals. Note that having three MO \mathbf{X} matrices also implies three distinct \mathbf{S} matrices, with similar notation. Of course each MO distribution may (and should) be fit independently. In this work, we employ a pivoted low-rank Cholesky decomposition of \mathbf{S} , and the explicit inverse is replaced by two triangular solves (on each side). It is important that the \mathbf{V} matrix obtained this way be explicitly symmetrized, as the values of “less important” elements are poorly determined numerically. Determining \mathbf{V} from the exact AO or MO integrals scales as $\mathcal{O}(N^5)$, where N is a measure of the system size, not considering sparsity. Using density-fitted integrals³¹ (or RI/CD integrals^{32–34}) reduces this to $\mathcal{O}(N^4)$.

In order to employ the LS-THC factorization in MP2, an additional approximation must be made to eliminate the inseparability of the orbital energy denominators. This is commonly handled by the Laplace transform approach,²⁸ where a numerical quadrature is used,

$$x^{-1} = \int_0^\infty e^{-xt} dt \approx \sum_{l=1}^L w_l e^{-xt_l} \quad (x > 0)$$

$$-(\epsilon_a + \epsilon_b - \epsilon_i - \epsilon_j)^{-1} \approx - \sum_{l=1}^L g_a^l g_b^l g_i^l g_j^l$$

where w_l and t_l are the weights and abscissas of the quadrature, and $g_a^l = w_l^{1/4} e^{-\epsilon_a t_l}$, $g_i^l = w_l^{1/4} e^{\epsilon_i t_l}$. Only a small, constant number of quadrature points are required; in this work we use 9 points (cc-pVDZ) or 10 points (cc-pVTZ). The error introduced by the Laplace transform with this number of points is essentially negligible.

Now, the LS-THC-MP2 energy expression can be constructed,

$$E_{LS-THC-MP2} = -2 \sum_{abij} \sum_{RSTU=1}^{n_{ai}} \sum_{l=1}^L X_a^R X_i^R V_{RS} X_b^S X_j^S g_a^l g_b^l g_i^l g_j^l X_a^T X_i^T V_{TU} X_b^U X_j^U$$

$$+ \sum_{abij} \sum_{RSTU=1}^{n_{ai}} \sum_{l=1}^L X_a^R X_i^R V_{RS} X_b^S X_j^S g_a^l g_b^l g_i^l g_j^l X_a^T X_j^T V_{TU} X_b^U X_i^U$$

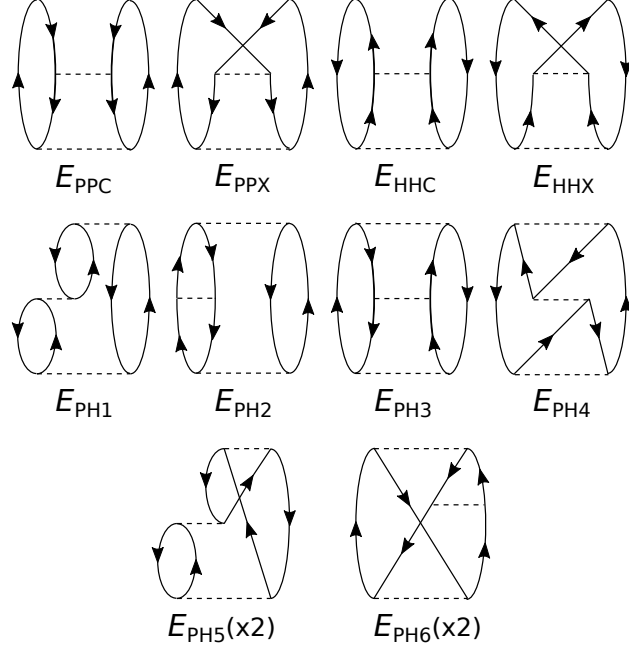


Figure 1. Goldstone diagrams for the MP3 energy and their associated energy contributions. The last two energy contributions include two diagrams each, related by a vertical reflection. Denominator lines are not shown for clarity.

$$= E_C + E_X$$

where \mathbf{X} and \mathbf{V} are both those specific to the ai and $abij$ MO distributions only, and the bounds on the MO summations are implicit. We have not shown the full factorization here; the first, Coulomb, term can be computed in $\mathcal{O}(N^3)$ time and the second, eXchange, term in $\mathcal{O}(N^4)$ time. Note that nearly all terms must be recomputed for each Laplace quadrature point, so that using fewer points will drastically reduce the running time.

The LS-THC-MP3 energy expression is significantly more involved, as there are 10 unique terms, depicted diagrammatically in Figure 1. As an example, consider the E_{PPC} term,

$$\begin{aligned}
E_{\text{PPC}} = 2 \sum_{abijef} \sum_{RSTU=1}^{n_{ai}} \sum_{VW=1}^{n_{ab}} \sum_{lm=1}^L & (X^{(ai)})_a^R (X^{(ai)})_i^R V_{RS}^{(abij)} (X^{(ai)})_b^S (X^{(ai)})_j^S \\
& \times g_a^l g_b^l g_i^l g_j^l (X^{(ab)})_a^V (X^{(ab)})_e^V V_{VW}^{(abcd)} (X^{(ab)})_b^W (X^{(ab)})_f^W \\
& \times g_e^m g_f^m g_i^m g_j^m (X^{(ai)})_e^T (X^{(ai)})_i^T V_{TU}^{(abij)} (X^{(ai)})_f^U (X^{(ai)})_j^U
\end{aligned}$$

Unlike in LS-THC-MP2, we must now deal with multiple distinct \mathbf{X} and \mathbf{V} matrices. The factorization of these equations can also be accomplished such that $\mathcal{O}(N^4)$ scaling is achieved,

and multiple such factorizations have been published in the literature. We use a different formulation that aims to minimize the number of $\mathcal{O}(N^4)$ steps while also minimizing memory usage and creating opportunities for index blocking and loop fusion. We have not included the full factored equations here as work on improved factorization is ongoing and the working equations are rapidly evolving. One of the largest obstacles to a practical implementation of LS-THC-MP3 is the introduction of two Laplace transform quadratures, which introduces an L^2 dependence into the computational cost. This cost multiplier ranges from $\sim 10\times$ (minimal number of points) to $\sim 100\times$ (this work).

Instead of including an explicit dependence on the orbital energy denominators in the MP3 energy, one can instead substitute the first-order cluster amplitudes, $\hat{T}_2^{[1]}$, and perform an LS-THC decomposition as for the two-electron integrals. Doing so completely removes the Laplace transform factors, but otherwise leaves the structure of the equations unchanged, e.g.,

$$\begin{aligned}
E_{\text{PPC}} = 2 \sum_{abijef} \sum_{RSTU=1}^{n_{ai}} \sum_{VW=1}^{n_{ab}} & (X^{(ai)})_a^R (X^{(ai)})_i^R T_{RS}^{[1]} (X^{(ai)})_b^S (X^{(ai)})_j^S \\
& \times (X^{(ab)})_a^V (X^{(ab)})_e^V V_{VW}^{(abcd)} (X^{(ab)})_b^W (X^{(ab)})_f^W \\
& \times (X^{(ai)})_e^T (X^{(ai)})_i^T T_{TU}^{[1]} (X^{(ai)})_f^U (X^{(ai)})_j^U
\end{aligned}$$

where the LS-THC decomposition of the amplitudes is given by,

$$(t^{[1]})_{ij}^{ab} \approx \sum_{RS=1}^{n_{ai}} (X^{(ai)})_a^R (X^{(ai)})_i^R T_{RS}^{[1]} (X^{(ai)})_b^S (X^{(ai)})_j^S$$

This simplification of the LS-THC-MP3 equations was simultaneously recognized by Lee et al.³⁵ Because this new method introduces an additional approximation of the cluster amplitudes (which were implicit and “exact” in the original formulation²⁰), the energy obtained will not be the same. We denote these two methods as LS-THC-MP3a and LS-THC-MP3b, respectively. A similar substitution can also be made for the LS-THC-MP2 energy, which reduces the cost (of $\mathcal{O}(N^4)$ steps) by a factor of L . We then denote LS-THC-MP2a and LS-THC-MP2b methods in a similar fashion. When there is little possibility of confusion, we will refer to these LS-THC methods simply as MP2a, MP3b, etc.

MP3, by itself, is not a particularly useful method. It suffers from intruder states and does not include the effect of higher-order excitations through the singles and doubles (e.g. from SDQ-MP4) or the infinite-order correlation effects of CI or CC. But, it is an important

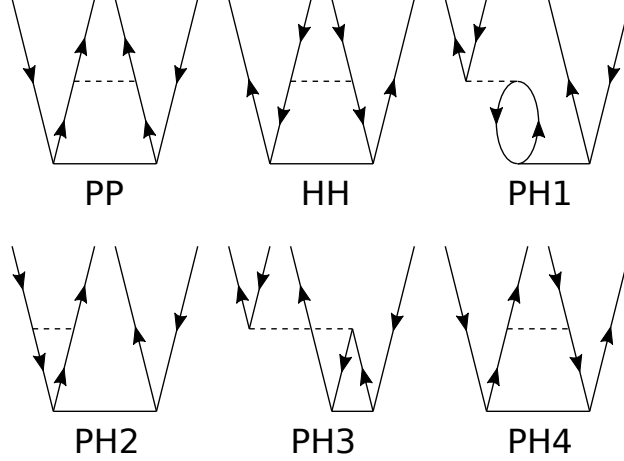


Figure 2. Open Goldstone diagrams for an LCCD iteration, or equivalently for determining the second-order amplitudes in MP3 (denominator lines not shown). Each term is labeled for ease of reference.

stepping stone to CC methods such as CCSD, as it captures the primary (linear) terms of the CCSD iteration. In fact, LCCD (also known as CEPA0³⁶) is simply an iterated version of MP3. The main difference is in the energy expression: while the full MP3 energy expression can be completely expanded as in MP3a, the LCCD (or general CC) energy must have the form of MP2b, where the first-order amplitudes are replaced by the converged ones. In each LCCD iteration, we must also directly solve for the updated cluster amplitudes. Thus, decomposition of the amplitudes is absolutely mandatory in moving to iterative methods.

In order to approximate this situation in MP3, we can reformulate the MP3 energy as a single iteration of LCCD: the starting amplitudes are the first-order ones, and the final amplitudes from which the energy are computed are simply the second-order ones. Each LCCD iteration comprises six open Goldstone diagrams, depicted in Figure 2. Note that we assume a canonical Hartree–Fock reference, and that the diagonal elements of the Fock matrix are included via the orbital energy denominators. These are open diagrams that, with division by the orbital energy differences, determine the updated (for MP3, second-order) amplitudes. Since we do not want to explicitly form the full amplitude tensor, we may insert a Laplace transform of the denominators and fit the result to an LS-THC form as above. Using the PP term as an example,

$$T_{RS}^{[2]} \leftarrow - \sum_{abefij} \sum_{TUVW=1}^{n_{ai}} \sum_{XY=1}^{n_{ab}} \sum_{l=1}^L S_{RT}^{-1} (X^{(ai)})_a^T (X^{(ai)})_i^T (X^{(ai)})_b^U (X^{(ai)})_j^U g_a^l g_b^l g_i^l g_j^l$$

$$\begin{aligned}
& \times (X^{(ab)})_a^X (X^{(ab)})_e^X V_{XY}^{(abcd)} (X^{(ab)})_b^Y (X^{(ab)})_f^Y \\
& \times (X^{(ai)})_e^V (X^{(ai)})_i^V T_{VW}^{[1]} (X^{(ai)})_f^W (X^{(ai)})_j^W S_{US}^{-1}
\end{aligned}$$

Each of these terms may also be factorized such that the scaling is at most $\mathcal{O}(N^4)$. Substituting $\mathbf{T}^{[2]}$ for $\mathbf{T}^{[1]}$ in the MP2b energy expression then gives a new variant of MP3 which we term MP3c.

Of course, the determination of the $\mathbf{T}^{[2]}$ matrix now has a dependence on L , which increases the cost considerably compared to MP3b. Instead, we may first fit the LCCD residual vector, and then perform the orbital energy weighting separately (again using the PP term as an example),

$$\begin{aligned}
Z_{RS} & \leftarrow \sum_{abefij} \sum_{TU=1}^{n_{ai}} \sum_{XY=1}^{n_{ab}} S_{RT}^{-1} (X^{(ai)})_a^T (X^{(ai)})_i^T (X^{(ai)})_b^U (X^{(ai)})_j^U \\
& \times (X^{(ab)})_a^X (X^{(ab)})_e^X V_{XY}^{(abcd)} (X^{(ab)})_b^Y (X^{(ab)})_f^Y \\
& \times (X^{(ai)})_e^V (X^{(ai)})_i^V T_{VW}^{[1]} (X^{(ai)})_f^W (X^{(ai)})_j^W S_{US}^{-1} \\
T_{RS}^{[2]} & = - \sum_{abij} \sum_{TU=1}^{n_{ai}} \sum_{l=1}^L S_{RT}^{-1} (X^{(ai)})_a^T (X^{(ai)})_i^T (X^{(ai)})_b^U (X^{(ai)})_j^U g_a^l g_b^l g_i^l g_j^l \\
& \times (X^{(ai)})_a^V (X^{(ai)})_i^V Z_{VW} (X^{(ai)})_b^W (X^{(ai)})_j^W S_{US}^{-1}
\end{aligned}$$

The second step only scales as $\mathcal{O}(N^3)$, and now the first step, which dominates the total cost, no longer depends on L . We denote this final, “double-fitted” variant as MP3d. The orbital weighting step is precisely the same as that for determining $\mathbf{T}^{[1]}$, except that \mathbf{Z} is inserted instead of $\mathbf{V}^{(abij)}$.

MP2b and MP3d are alike in that they both formulate the energy as a contraction between an approximate amplitude tensor and the Coulomb and exchange integrals,

$$\begin{aligned}
E_{n+1} & = -2 \sum_{abij} \sum_{RSTU=1}^{n_{ai}} X_a^R X_i^R T_{RS}^{[n]} X_b^S X_j^S X_a^T X_i^T V_{TU} X_b^U X_j^U \\
& + \sum_{abij} \sum_{RSTU=1}^{n_{ai}} X_a^R X_i^R T_{RS}^{[n]} X_b^S X_j^S X_a^T X_j^T V_{TU} X_b^U X_i^U
\end{aligned}$$

where n is either 1 (LS-THC-MP2b) or 2 (LS-THC-MP3d), and the $\mathbf{X}^{(ai)}$ grid is assumed. Furthermore, we can explicitly write the $\mathbf{T}^{[n]}$ core matrix in each case by LS-THC fitting of either the integrals or the LCCD residual, respectively,

$$E_{n+1} = -2 \sum_{abij} \sum_{RSTU=1}^{n_{ai}} \left(\sum_{efmn} \sum_{VWXY=1}^{n_{ai}} \sum_{l=1}^L X_e^V X_m^V Z_{VW}^{[n]} X_f^W X_n^W g_e^l g_f^l g_m^l g_n^l \right)$$

$$\begin{aligned}
& \times X_e^X X_m^X X_f^Y X_n^Y S_{XR}^{-1} S_{YS}^{-1} \Bigg) X_a^R X_i^R X_b^S X_j^S X_a^T X_i^T V_{TU} X_b^U X_j^U \\
& + \sum_{abij} \sum_{RSTU=1}^{n_{ai}} \left(\sum_{efmn} \sum_{VWXY=1}^{n_{ai}} \sum_{l=1}^L X_e^V X_m^V Z_{VW}^{[n]} X_f^W X_n^W g_e^l g_f^l g_m^l g_n^l \right. \\
& \left. \times X_e^X X_m^X X_f^Y X_n^Y S_{XR}^{-1} S_{YS}^{-1} \Bigg) X_a^R X_i^R X_b^S X_j^S X_a^T X_j^T V_{TU} X_b^U X_i^U
\end{aligned}$$

where the parentheses group $\mathbf{T}^{[n]}$, and $\mathbf{Z}^{[n]}$ is either \mathbf{V} ($n = 1$) or \mathbf{Z} ($n = 2$). From this form, we can regroup quantities and arrive at a different, but numerically equivalent interpretation,

$$\begin{aligned}
E_{n+1} &= -2 \sum_{efmn} \sum_{VWXY=1}^{n_{ai}} \sum_{l=1}^L X_e^V X_m^V Z_{VW}^{[n]} X_f^W X_n^W g_e^l g_f^l g_m^l g_n^l X_e^X X_m^X X_f^Y X_n^Y \\
& \times \left(\sum_{abij} \sum_{RSTU=1}^{n_{ai}} S_{XR}^{-1} S_{YS}^{-1} X_a^R X_i^R X_b^S X_j^S X_a^T X_i^T V_{TU} X_b^U X_j^U \right) \\
& + \sum_{efmn} \sum_{VWXY=1}^{n_{ai}} \sum_{l=1}^L X_e^V X_m^V Z_{VW}^{[n]} X_f^W X_n^W g_e^l g_f^l g_m^l g_n^l X_e^X X_m^X X_f^Y X_n^Y \\
& \times \left(\sum_{abij} \sum_{RSTU=1}^{n_{ai}} S_{XR}^{-1} S_{YS}^{-1} X_a^R X_i^R X_b^S X_j^S X_a^T X_j^T V_{TU} X_b^U X_i^U \right) \\
& = -2 \sum_{efmn} \sum_{VWXY=1}^{n_{ai}} \sum_{l=1}^L X_e^V X_m^V Z_{VW}^{[n]} X_f^W X_n^W g_e^l g_f^l g_m^l g_n^l X_e^X X_m^X V_{XY} X_f^Y X_n^Y \\
& + \sum_{efmn} \sum_{VWXY=1}^{n_{ai}} \sum_{l=1}^L X_e^V X_m^V Z_{VW}^{[n]} X_f^W X_n^W g_e^l g_f^l g_m^l g_n^l X_e^X X_m^X \tilde{V}_{XY} X_f^Y X_n^Y
\end{aligned}$$

In the first term, refitting \mathbf{V} is an idempotent operation. In fact, the Coulomb term for MP2b is precisely equal to that in MP2a (except for the introduction of additional accumulated round-off error). However, in the second term, we have now performed a refitting of \mathbf{V} , but in the exchange ordering. Thus, we are attempting to fit a purely non-local operator with an LS-THC decomposition. Even if \mathbf{Z} were a purely local operator (as in MP2b), we would still experience error due to this exchange fitting. Because all iterative CI and CC methods have an energy expression of this form, they will all necessarily experience an “exchange fitting error”, although numerical results below show that the effect is not necessarily uniform.

We should make one final note about the grids used. The Cholesky decomposition-based pruning procedure in Ref. 30 naturally produces grids of different sizes for each of the three MO pair distributions from the same parent grid. The size of the final grids is controlled by

varying a cutoff parameter ϵ , or conversely by fixing ϵ and varying the parent grid size. We use the latter approach here (except for the results in Figure 9), with a fixed $\epsilon = 10^{-5}$. The size of the parent grid is specified by the integer triplet (L_{max}, N_1, N_H) , where L_{max} is the highest angular momentum for which any of the angular grids is an exact quadrature, N_1 specifies the number of radial quadrature points for first-row atoms, and N_H specifies the number of radial quadrature points for hydrogen atoms. All other aspects of constructing the grids are detailed in Ref. 30.

III. RESULTS AND DISCUSSION

In order to understand the intrinsic errors associated with each LS-THC-MP2 and LS-THC-MP3 variant, we performed a series of calculations on regular test systems of increasing size: water clusters, linear alkanes, and linear alkenes, each with up to 40 first-row atoms. Density fitting was used for the reference calculations as well as the LS-THC calculations (so that, technically, these are LS-DF-THC calculations). Previous work has shown that the density fitting and LS-THC errors are essentially additive,²¹ so we consider the $E_{\text{LS-THC-DF}} - E_{\text{DF}}$ difference to be representative of the true LS-THC error. MP3a, MP3c, and canonical MP3 (without density fitting) calculations were only completed through systems with 20 first-row atoms. MP3 errors are for the MP3 contribution to the correlation energy only (i.e. excluding the MP2 energy). The cc-pVDZ basis set³⁷ was used for all calculations except where indicated, and the frozen core approximation was used throughout. Corresponding cc-pVXZ-RI auxiliary basis sets³⁸ were used for the correlation energy. Unless otherwise noted, a (7,19,11) parent grid was used with $\epsilon = 10^{-5}$ (for comparison, the common SG-1 grid³⁹ is roughly similar to the much larger (23,51,43) grid as used in this work). In all cases point group symmetry is not used, except for determining the orientation of the molecule. All calculations (including DF-MP2 and DF-MP3) were performed with a development version of CFOUR.⁴⁰ We initially tried to use other packages for the density-fitting calculations, but were unable to compete calculations on the larger systems due to limitations of the 32-bit BLAS interface used.

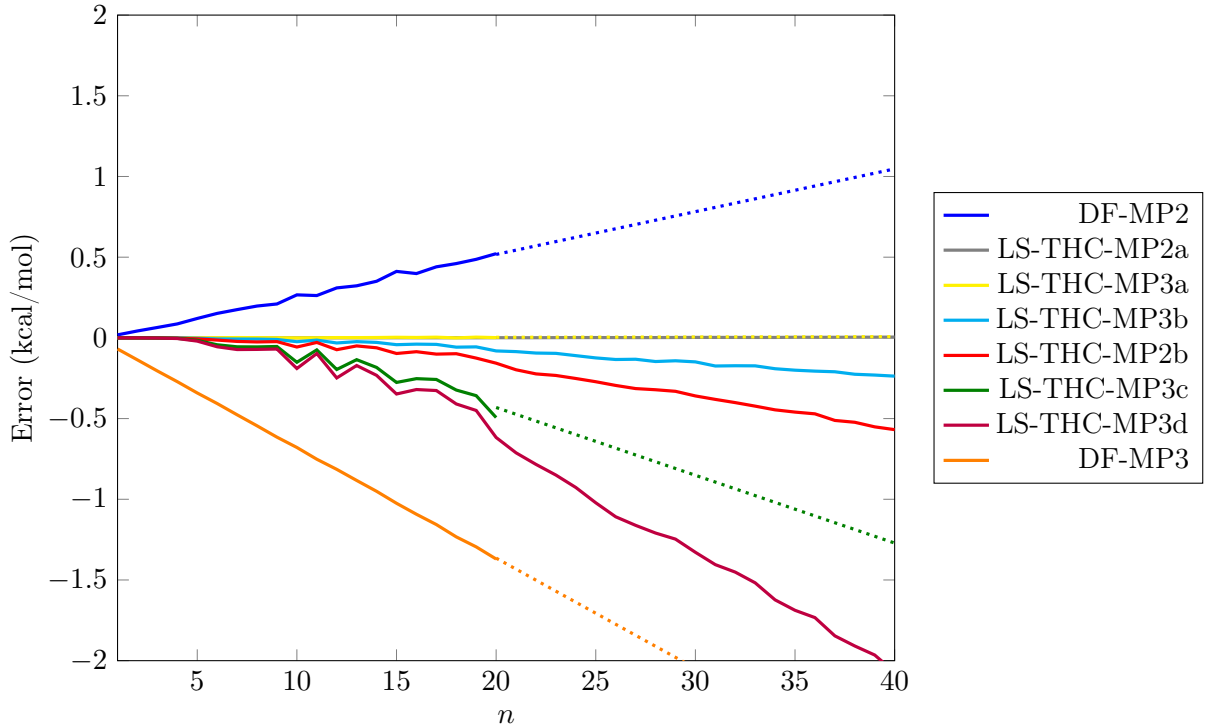


Figure 3. Errors for water clusters, $(\text{H}_2\text{O})_n$. Note that legend entries are given in the same order as the error values at $n = 20$, and that the curves for LS-THC-MP2a and LS-THC-MP3a essentially lie along the x -axis. Errors for LS-THC-MP3a, LS-THC-MP3c, and for standard density fitting are extrapolated to $n = 40$ from the linear region of the curves.

A. Water Clusters

Density fitting and LS-THC errors for water clusters are depicted in Figure 3. Density fitting errors are exceptionally linear, and error cancellation between the DF-MP2 and DF-MP3 correlation energy contributions leads to a rather modest total correlation energy error of approximately -8 micro-Hartree per correlated electron. MP2a and MP3a errors are, for the grid size used, below 0.005 kcal/mol—an entirely negligible amount. It is clear that rather smaller grids could be used for these calculations (although LS-THC-MP3a is not efficient due to its dependence on L^2) while still maintaining manageable errors. The hand-optimized grid of Ref. 24 is indeed smaller than the grid used here, but based on additional results below, it seems likely that even smaller grids could be used if they are appropriately pruned from a large starting grid. Since MP2 is not a focus of this work we defer such a determination to future work.

The LS-THC methods that include factorization of the first- and/or second-order doubles amplitudes display larger errors, but still roughly in line with the errors due to density fitting. These errors are noticeably less linear with increasing system size, especially for the smaller clusters. MP3b is the most stable, and the error is quite small, with approximately 0.25 kcal/mol error ($7\times$ smaller than the density-fitting error) at $(\text{H}_2\text{O})_{40}$. Approximation of the second-order amplitudes in MP3c and MP3d, or likewise approximation of the first-order amplitudes in MP2b incurs larger errors, but still of a manageable size. The similarity of the MP3c and MP3d errors shows that double-fitting does not introduce a significant additional error. Interestingly, the LS-THC-MP3 errors seems to follow separate linear trends above and below $(\text{H}_2\text{O})_{20}$. This may be explained by the fact that larger clusters are poorly-representative of isolated molecular clusters, including many “broken” hydrogen bonds, etc. The error seems to be larger in this case, possibly indicating that LS-THC-MP3 (with factorization of the amplitudes) is less effective at capturing the remaining dispersion interactions compared to stronger effects such as hydrogen bonding.

B. Linear Alkanes

Linear alkane geometries were generated with fixed bond lengths and angles, in order to provide a highly systematic aliphatic benchmark. The increased linearity of the errors in Figure 4 compared to Figure 3 seems to reflect this situation. However, there are interesting deviations between the even- and odd-numbered chains for LS-THC-MP3, and to a much more minor extent, MP2b. These chains have point group symmetry C_{2v} and C_{2h} , respectively, and slightly different standard orientations. We posit that this difference in orientation (relative to the axis-fixed molecular grid) is responsible for the different errors, especially with respect to the $\mathbf{X}^{(ab)}$ grid. Nonetheless, within each class the errors are highly linear, and of very similar magnitudes as in the case of water clusters. The biggest exception is MP3a, which now displays a non-negligible error very similar to that of MP3b. Below, we show that this is due to imbalance between the different grids, and is not indicative of degraded performance of MP3a specifically. Note that in these systems, the errors due to the DF-MP2 and DF-MP3 energy corrections are additive, with a total correlation error of approximately 25 micro-Hartree per correlated electron. In this case, we also see very similar errors between MP2b and MP3c/MP3d. It is tempting to expect similar errors based on the

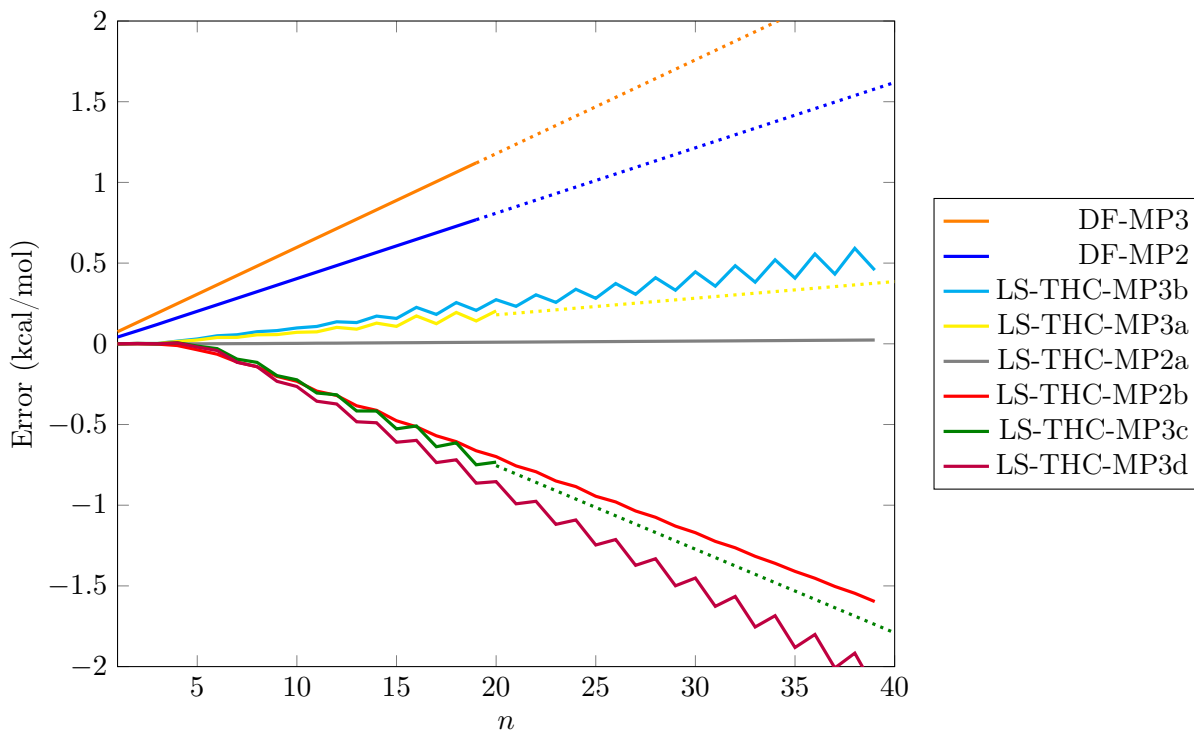


Figure 4. Errors for linear alkanes, C_nH_{2n+2} . Note that legend entries are given in the same order as the error values at $n = 20$, and that the curve for LS-THC-MP2a essentially lies along the x -axis. Errors for for LS-THC-MP3a, LS-THC-MP3c, and for standard density fitting are extrapolated to $n = 40$ from the linear region of the curves. Data not available for $n = 40$.

realization that, in these methods, we are equivalently making an LS-THC approximation of the exchange integrals. However, results for both water clusters and linear alkenes (next section) show no such agreement. Instead, the numerical effect of the LS-THC approximation on the exchange integrals seems to depend on the quantity that it is multiplied by, either the first- or second-order amplitudes in MP2b and MP3c/MP3d, respectively. These amplitudes must then “sample” different portions of the exchange integral tensor.

C. Linear Alkenes

Linear (all-E) alkene geometries were also constructed with fixed bond lengths and angles. The errors are depicted in Figure 5, and overall show essentially the same trends as for linear alkanes, except that now all systems are the same symmetry and so there are no issues with orientation. The only substantive differences are that a) the MP3a/MP3b errors are of the

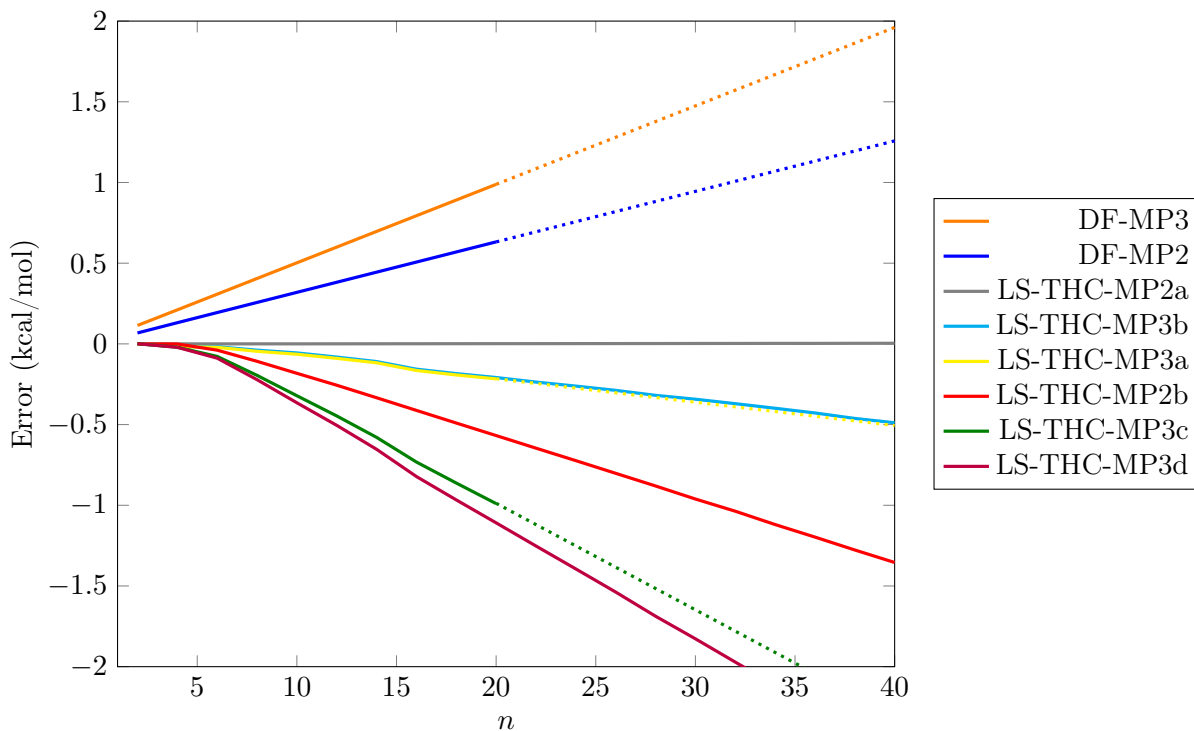


Figure 5. Errors for linear alkenes, C_nH_{n+2} . Note that legend entries are given in the same order as the error values at $n = 20$, and that the curve for LS-THC-MP2a essentially lies along the x -axis. Errors for LS-THC-MP3a, LS-THC-MP3c, and for standard density fitting are extrapolated to $n = 40$ from the linear region of the curves.

opposite sign (but similar magnitude), and b) the MP2b error is somewhat smaller, and more in line proportionately with the results for water clusters. The similar magnitude of all LS-THC errors for alkenes compared to alkanes is encouraging, as it shows that LS-THC-MP3 does not experience any particular issues due to extensive electron delocalization. This highlights the advantage of maintaining a coherent approximation of the global Hamiltonian and/or wavefunction as opposed to approaches based on fragmentation. For alkenes, as for the other two sets of test systems, the LS-THC errors are seen to be highly linear, but with an interesting “threshold” effect. The errors for all THC-MP3 methods are essentially zero below 20–25 correlated electrons. We attribute this to crossover between the grid size used (which scales linearly with molecular size) and the “exact” grid size, that is the size of grid needed to exactly represent the original tensors (which scales quadratically with molecular size). The ramifications of this effect are explored in the next section.

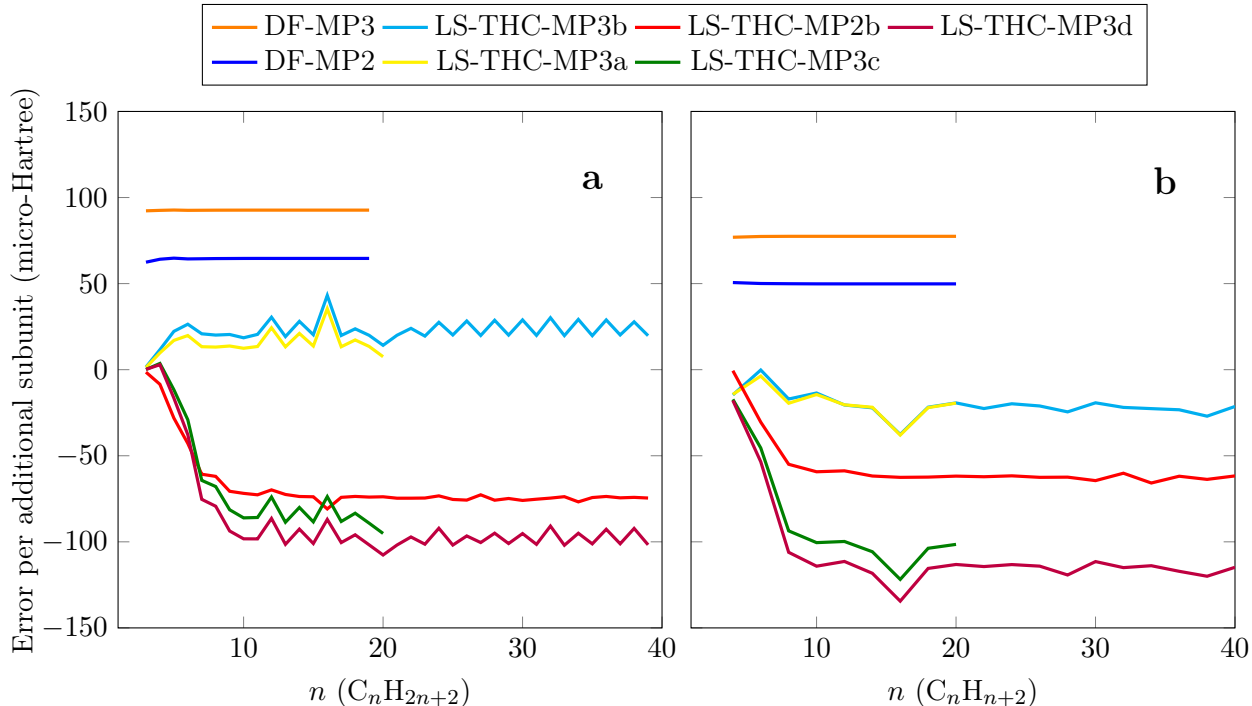


Figure 6. Incremental errors for each additional CH_2 (alkanes) or $\frac{1}{2}\text{C}_2\text{H}_2$ (alkenes) subunit. Note that legend entries are given in the same order as the error values at $n = 20$. For both alkenes (a) and alkanes (b), the difference between error values at n and $n - 2$, divided by 2, was used as the incremental error (see text for details).

D. Size-Extensivity and Size-Consistency

While canonical MP2 and MP3 are manifestly size-extensive due to the linked structure of their diagrammatic representations, it is possible for size-extensivity error to be introduced by further approximations. In particular, since the LS-THC decomposition reduces the quadratic pair molecular orbital space to a linear grid representation, we might expect a non-linear size dependence to the incurred error and hence a loss of size-extensivity. We have numerically measured the size-extensivity characteristics of the methods used via the synthetic alkane and alkene benchmarks. For each type of system, since all bond angles and distances are fixed, the asymptotic effect of introducing a further subunit (CH_2 for alkenes, C_2H_2 for alkenes) should be a constant increase in correlation energy. Thus, if we compute the difference between successive correlation energies as we increase the number of subunits, we should observe an asymptotically constant value. We further break down the successive

Method	Threshold		Size-Consistency Error		Incremental Error	
	(electrons)		(kcal/mol)		(micro-Hartree/electron)	
DF-MP2	0	-1	0.00	-0.01	10.8	10.0
DF-MP3	-2	-2	-0.02	-0.02	15.5	15.5
LS-THC-MP2a	36	45	0.00	0.00	0.2	0.0
LS-THC-MP2b	29	27	-0.23	-0.21	-12.4	-12.4
LS-THC-MP3a	20	25	0.04	-0.07	3.0	-4.6
LS-THC-MP3b	18	27	0.04	-0.08	3.9	-4.5
LS-THC-MP3c	33	25	-0.28	-0.33	-13.8	-21.0
LS-THC-MP3d	33	24	-0.34	-0.36	-16.4	-23.2

Table I. Size-extensivity characteristics as measured by linear extrapolation of alkane and alkene chains. The first value in each column is for alkanes, while the second is for alkenes.

energy differences by computing the difference between DF and LS-THC errors of successive systems, so that any size-extensivity error (which the canonical method does not have) will be magnified and readily evident. Such curves are depicted in Figure 6. For alkanes, we have separately computed differences between even- and odd-numbered chains and then divided by two in order to eliminate the orientation problem. Likewise, the alkene energy differences have been divided by two to put them on an equal footing (i.e. we use a $\frac{1}{2}\text{C}_2\text{H}_2$ subunit).

From this figure, we do indeed see that all methods reach an essentially constant incremental energy value. For DF-MP2 and DF-MP3, the convergence to this value is extremely rapid and stable. For other methods, the steady-state value is only reached for 10 or more carbon atoms. This is a consequence of the threshold effect observed in previous sections. Thus, both density fitting and LS-THC are size-extensive as they display the correct asymptotic behavior. Despite the asymptotic behavior, the threshold effect does indeed imply a small size-consistency error. In Table I, we estimate this error as the negative of the y intercept for a linear fit of the errors in Figure 4 and Figure 5 (only values for $n \geq 8$ were used in the fit). The x intercept of this line is taken as the threshold value (as a number of correlated electrons), while the slope gives the asymptotic incremental error values. The y intercept is essentially the anomalous energy extrapolated to an empty system; we take its negative to indicate the expected error in a reaction like $\text{A} + \text{B} \rightarrow \text{AB}$. In fact, we have also numerically

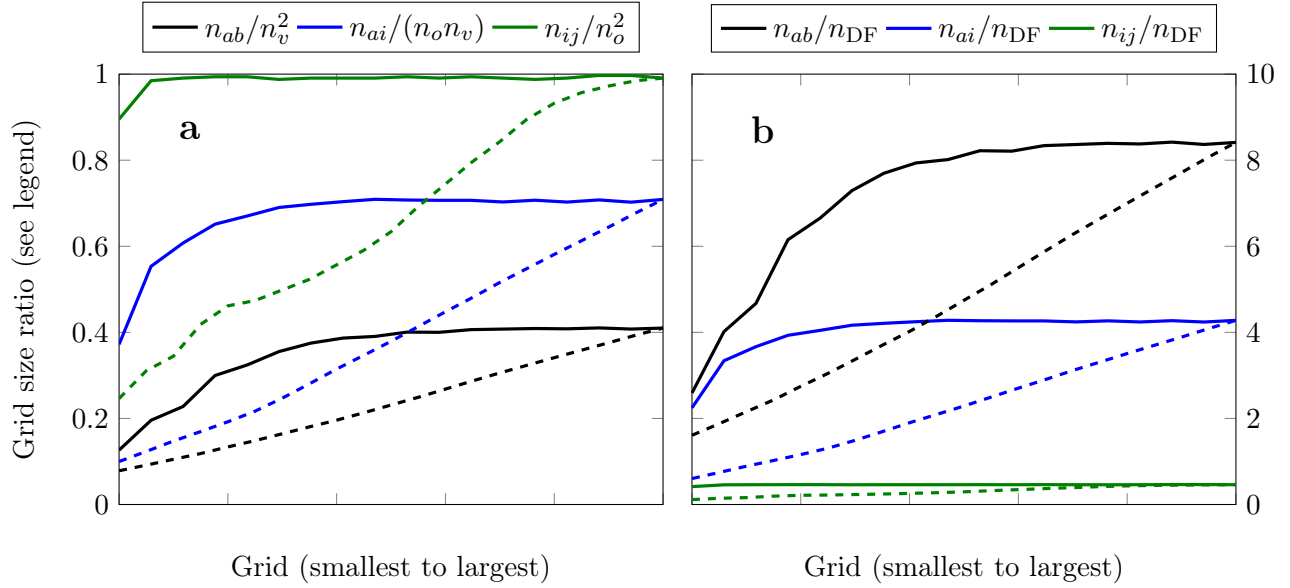


Figure 7. Grid size ratios for each of the three pruned grids (specific to the ab , ai , and ij MO distributions), varying the size of the parent grid from (7,19,11) to (23,51,43) with a fixed cutoff $\epsilon = 10^{-5}$ (solid lines, the hand-optimized grid of Ref. 24 is also included), and varying ϵ logarithmically from 10^{-1} to 10^{-5} in steps of 0.2 log units with a fixed (23,51,43) parent grid (dotted lines). In (a) the grid size ratios are given w.r.t. the full size of the MO distributions, and in (b) the ratios are given w.r.t. the number of density fitting functions, n_{DF} .

confirmed this error by performing a super-system calculation of two octane molecules separated by 100 Å. The error in comparison to twice the energy of a single octane molecule closely matches the estimated values. However, it is critically important to note that, unlike in truncated CI methods, this size-consistency error is fixed and does not grow with system size. From Table I, we can also see that the threshold effect impacts MP2a and MP3a, which do not feature LS-THC decomposition of the amplitudes. While the size-consistency errors are very small in these cases, they are non-zero and should not be disregarded. For consistency we have also computed threshold values and size-consistency errors for DF-MP2 and DF-MP3 in the same manner; all values are essentially zero as expected.

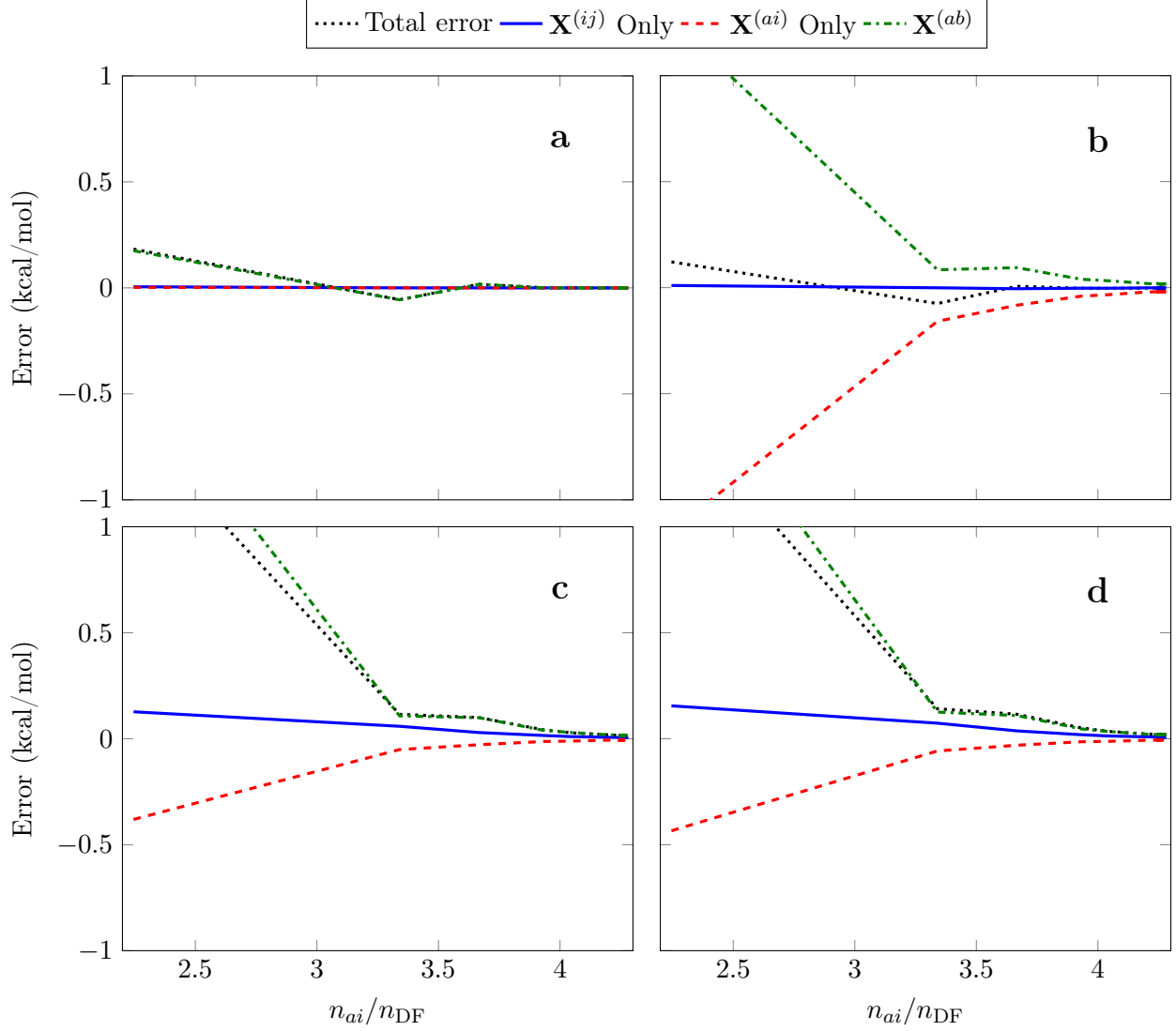


Figure 8. Errors in the total LS-THC-MP3 energy correction and for select energy components for (a) LS-THC-MP3a, (b) LS-THC-MP3b, (c) LS-THC-MP3c, and (d) LS-THC-MP3d, as the parent grid is varied and with fixed $\epsilon = 10^{-5}$. The energy components are labeled by which collocation matrices appear in the expression for the middle Hamiltonian vertex: “ $\mathbf{X}^{(ij)}$ Only” refers to $E_{\text{HHC}} + E_{\text{HHX}}$, “ $\mathbf{X}^{(ai)}$ Only” to $E_{\text{PH1}} + E_{\text{PH4}} + E_{\text{PH5}}$, and “ $\mathbf{X}^{(ab)}$ ” to $E_{\text{PPC}} + E_{\text{PPX}} + E_{\text{PH2}} + E_{\text{PH3}} + E_{\text{PH6}}$. Note that in the latter case $\mathbf{X}^{(ij)}$ appears as well in some terms, but the error due to $\mathbf{X}^{(ab)}$ is expected to dominate.

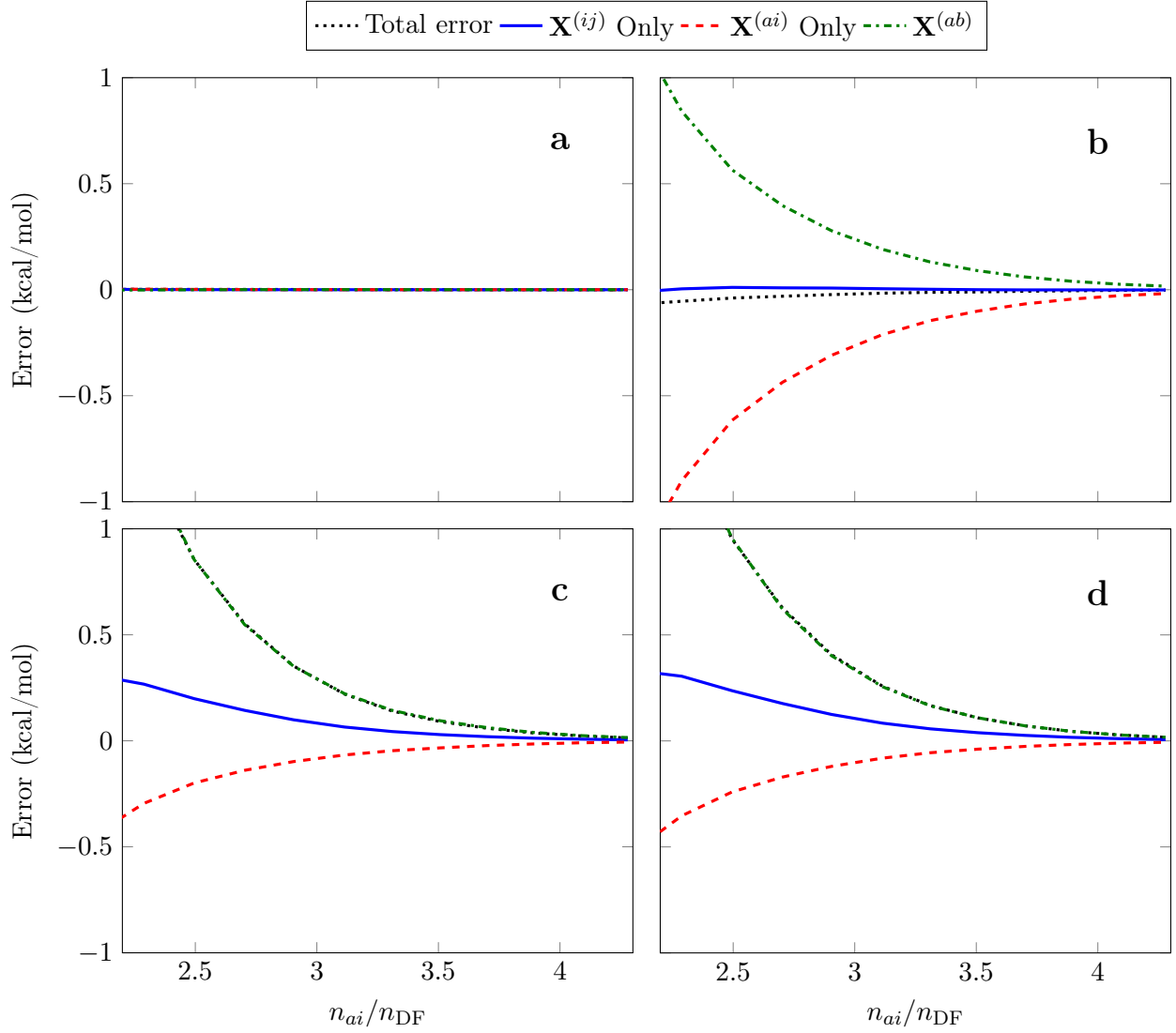


Figure 9. Errors in the total LS-THC-MP3 energy correction and for select energy components for (a) LS-THC-MP3a, (b) LS-THC-MP3b, (c) LS-THC-MP3c, and (d) LS-THC-MP3d, as ϵ is varied logarithmically between 10^{-1} and 10^{-5} with fixed (23,51,43) parent grid. The energy components are labeled by which collocation matrices appear in the expression for the middle Hamiltonian vertex.

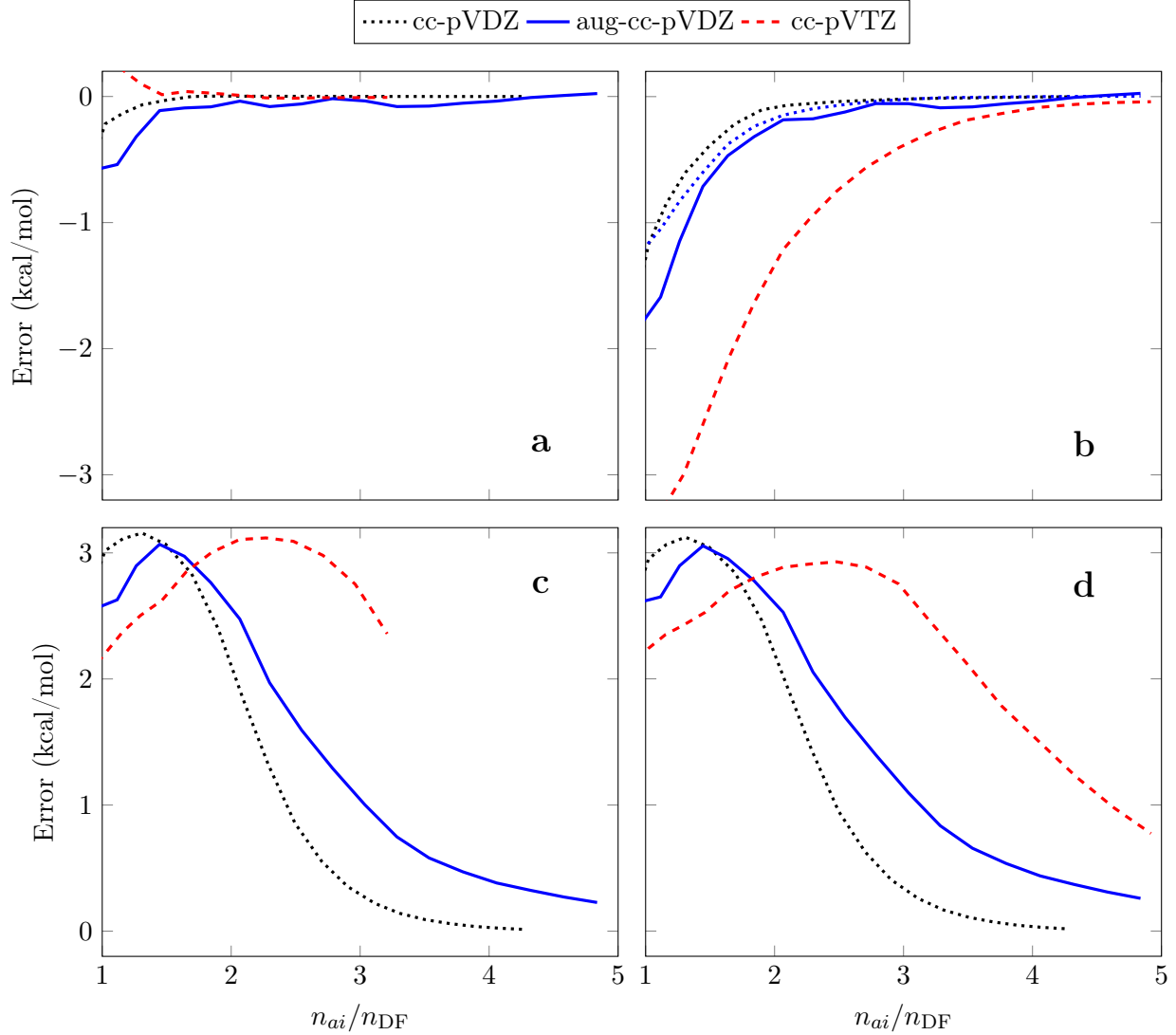


Figure 10. Basis set dependence of the total LS-THC-MP3 error using grids determined as in Figure 9: (a) LS-THC-MP3a, (b) LS-THC-MP3b, (c) LS-THC-MP3c, (d) LS-THC-MP3d. The blue dotted line in (b) is the difference between the MP3b and MP3a energies with aug-cc-pVDZ (see text).

E. Grid and Basis Set Dependence

The tests in the preceding section all used a fixed grid and pruning cutoff (ϵ) value. This grid was chosen to balance error and computational efficiency (see next section), but it is instructive to evaluate a wider range of grids, in particular for LS-THC-MP3 methods other than MP3a. We use octane for all experiments in this section as it is large enough to

overcome the error threshold behavior, but small enough to experiment with large grids and larger basis sets. In Figure 7 the essential size characteristics of two sets of grids are depicted as applied to octane, using “grid size ratios”, or the number of grid points as a fraction of the total (quadratic) pair molecular orbital space (left sub-figure) or the number of density fitting functions (right sub-figure). The solid lines correspond to a set of 17 regular parent grids of increasing size, from (7,19,11) to (23,51,43), with a fixed cutoff of $\epsilon = 10^{-5}$. The largest grid is similar in size to the SG-1 grid which is commonly used in DFT calculations. In addition, we have included Grid 0, which is the hand-optimized grid of Ref. 24. The grid size ratios depicted in Figure 7 are for the cc-pVDZ basis set; we use the same grids for the cc-pVTZ studies later in this section although of course the grid size ratios are smaller except for the ij distribution. Additionally, we have used a set of 21 grids prepared by taking the (23,51,43) parent grid and varying ϵ logarithmically between 10^{-1} and 10^{-5} ; the grid size ratios are depicted by the dashed lines.

In Figure 8 the errors for MP3a–MP3d are depicted with respect to the ai grid size ratio. In addition to the total error in the MP3 energy correction, we have split the error into three terms depending on which grids are involved. In particular, we split out grids that depend only on $\mathbf{X}^{(ij)}$ in the central Hamiltonian vertex, as we expect this term to be very small based on the grid size ratios in Figure 7. We then split the remaining terms into those which depend on $\mathbf{X}^{(ab)}$ and those that do not (“ $\mathbf{X}^{(ai)}$ only”), as the ab grid is the most incomplete based on the size ratios. The MP3a errors are all quite small, with only the $\mathbf{X}^{(ab)}$ error reaching a significant level. Individual error components (except the $\mathbf{X}^{(ij)}$ only terms) for MP3b are significantly larger, with errors as large or larger than 1 kcal/mol. However, these errors efficiently cancel, leaving a total MP3b error very similar to that of MP3a. Individual error components for MP3c and MP3d are of a similar magnitude to MP3b, but do not cancel completely. There is some error cancellation in this case, though, now between the $\mathbf{X}^{(ij)}$ only (no longer insignificant) and $\mathbf{X}^{(ai)}$ only terms. This leaves the total error essentially equal to the $\mathbf{X}^{(ab)}$ error.

As the grids become larger, the MP3a errors essentially go to zero, as was observed previously for LS-THC-MP2. The MP3b total error also becomes quite small, although measurably non-zero. In contrast, the individual error components, as well as total MP3c and MP3d errors do not go to zero in the range of grid sizes tested, and remain in the vicinity of 0.01–0.02 kcal/mol for the largest grids used. While this error is of course quite small, it

is a critical difference in comparison to MP2a and MP3a: the LS-THC error for non-local operators is typically larger and more slowly-decaying than for local operators. The error cancellation properties of the various methods are readily apparent for large grids, but are somewhat less reliable for the smaller grids. Especially in the case of MP3b, this sharply limits the accuracy for smaller parent grids.

Errors using the second set of grids are depicted in Figure 9. Here, the behavior for large grids is essentially the same as before, and so is not emphasized. In contrast to the case of varying the parent grid, keeping a large parent grid and instead varying ϵ seems to result in much smoother and more orderly error trends. Most importantly, we can see that for grid sizes similar to the smaller grids in Figure 8 (e.g. Grids 1–4), the error cancellation properties are much better preserved. This has the effect of drastically reducing the total error for MP3b even with similar pruned grid sizes. For very small grids, the error cancellation properties do again break down, but very small errors for MP3a and MP3b are still achievable. Looking at the comparison of grid size ratios in Figure 7, it seems clear that the technique of controlling grid size via ϵ results in *ab*, *ai*, and *ij* grids that are mutually balanced and provide the greatest opportunity for effective error cancellation. The mechanism of error cancellation in MP3b is not well understood, except that we can note that, unlike MP3c, MP3d, as well as MP2b, the energy expression is not written as a contraction between a set of amplitudes and the Hamiltonian. In that case, we noted that approximating the amplitudes is equivalent to instead approximating the exchange integrals which might be expected to have rather severe numerical effects. Instead, MP3b may better represent the effect of approximating $\mathbf{T}_2^{[1]}$ alone, without invoking any such approximation of the exchange integrals. While $\mathbf{T}_2^{[1]}$ is still non-local (and hence leads to a non-zero MP3b error even with large grids), the non-locality seems to be fairly limited, at least in these examples.

Finally, we examine errors with the larger aug-cc-pVDZ and cc-pVTZ basis sets in Figure 10, using the second set of grids (varying ϵ). Here, apart from the small error for aug-cc-pVDZ which we attribute to grid imbalance (most likely the parent grid requires larger atomic radii to better represent the diffuse functions), the MP3a error is essentially the same as for cc-pVDZ (that is to say, quite small). For MP3b, the errors for cc-pVTZ are approximately $5\times$ larger in the small to intermediate grid size regime. In the large grid limit, however, errors are $40\text{--}50\times$ larger. On the other hand, errors for aug-cc-pVDZ are essentially the same. This is especially apparent when one considers $E_{\text{MP3b}} - E_{\text{MP3a}}$ (blue

dotted line) which cancels out the error due to grid imbalance. While MP3b still enjoys quite effective error cancellation, using a larger grid has a rather extreme effect on the MP3c and MP3d total energy errors, which are $\sim 45\times$ larger in the large grid limit (~ 0.75 kcal/mol). Decreasing ϵ only provides limited improvement (for cc-pVTZ the error may be decreased moderately to 0.33 kcal/mol), as values below $\sim 2 \times 10^{-6}$ result in divergence due to the increasingly-poor condition number of S . Thus, even with a very large and hence inefficient grid, MP3c and MP3d with cc-pVTZ are limited in accuracy to tens of micro-Hartree error per excess correlated electron. aug-cc-pVDZ errors are intermediate, but especially in comparison to MP3b still rather large. Of course, this error is due to non-locality of the amplitudes (and/or the exchange integrals!). The massive increase in the MP3b error upon going from cc-pVDZ to cc-pVTZ, but not when going to aug-cc-pVDZ, suggests that the angular completeness of the orbital basis set is a driving factor. Including higher-angular momentum basis functions leads to a better description of angular electron correlation; this is a short-range yet non-local effect that is not well-represented by LS-THC. While longer-range non-local effects of course still exist (in particular dispersion), these short-range effects seem to dominate based on these experiments. This is good news for MP3b as short-range locality should be possible to include via a multiplicatively-separable geminal grid that still scales linearly with molecular size. For MP3d, such a grid would perhaps improve the errors but is unlikely to substantially eliminate them, as the increase in error for aug-cc-pVDZ indicates longer-range non-local errors. However, the $E_{\text{MP3d}} - E_{\text{MP3b}}$ energy difference may provide a correction factor for similar errors in iterative LS-THC methods.

F. Timings

While we have shown that LS-THC-MP3 errors may be made acceptably small while using rather compact grids, these methods are not useful in practice unless they can also achieve a speedup over canonical calculations. Of course, the argument with all reduced-scaling methods is that the reduced-scaling version will “eventually” be faster for large enough molecules, but how large does the molecular system need to be? In Figure 11 we report timings for the water cluster calculations analyzed in section III A for all LS-THC-MP3 methods, as well as for DF-MP3. The timings reported only include the actual MP3 correlation energy calculation (and MP2, which is a negligible component w.r.t. timings) and, for the LS-THC-MP3

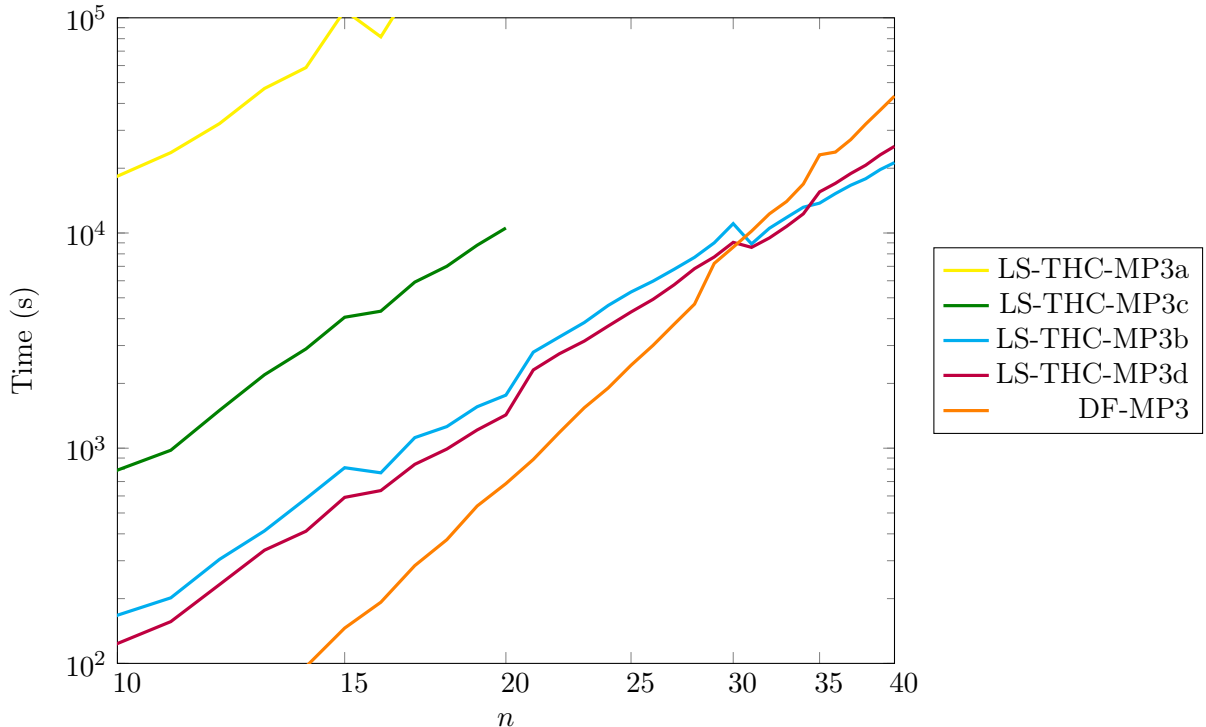


Figure 11. Timings for DF- and LS-THC-MP3 methods for water clusters, $(\text{H}_2\text{O})_n$ with cc-pVDZ. Both axes are on a logarithmic scale to highlight the polynomial scaling of each method. Legend entries are given in the order of the timings at $n = 20$.

calculations, the time to construct the grids and factorize the integrals. All calculations were performed using a single node with 2x Intel Xeon E5-2695v4 CPUs and either 256 or 768 GiB of memory; OpenMP was used to parallelize the calculation over all 36 cores. The figure utilizes log-log scaling of the axes, which reveals the reduced-scaling nature of LS-THC-MP3 relative to DF-MP3. Here, the MP3b and MP3d calculations, which have very similar computational costs, become cheaper (reach crossover) around 240 correlated electrons. Timings for alkanes and alkenes (not shown) exhibit a similar crossover point. While the observed crossover point is not as small as one might hope, these results are indeed encouraging from the standpoint of a practical LS-THC implementation, not only of MP3 but of more elaborate methods such as CCSD as well. The time required to construct the grids and perform the initial fit of the integrals ranges from 3% of the total ($n = 40$) to 10% of the total ($n = 10$). We expect further developments in reducing the grid sizes and in improving the factorization and implementation of LS-THC-MP3 to decrease the crossover point.

As a point of reference, the OSV-PNO-MP3 method of Hättig et al.,² which is similar to LS-THC-MP3 in that it scales as $\mathcal{O}(N^4)$ and does not utilize orbital sparsity or domain localization, has a crossover point with canonical MP3/cc-pVDZ at about 60 correlated electrons. For LS-THC-MP3 to achieve the same crossover, a speedup of approximately $10\times$ would be required. Through a combination of improved factorization, code optimization, and reduced grid sizes, we believe this is an eminently achievable goal; in this regard it seems clear that both THC- and PNO-based decompositions offer a path to efficient and effective reduced-scaling electronic structure methods, although with very distinct theoretical and computational approaches.

IV. CONCLUSIONS

By applying several LS-THC-MP2 and LS-THC-MP3 variants to water cluster, linear alkane, and linear alkene tests systems, we observe a number of trends that support the following conclusions:

1. With the cc-pVDZ basis set, only relatively small molecular grids (a few hundred points per atom) are necessary to obtain LS-THC-MP3 errors similar to or smaller than errors due to density fitting. Errors for MP2a and MP2b are essentially negligible with such grid sizes when using balanced grids.
2. Going from cc-pVDZ to cc-pVTZ significantly increases errors for MP2b, MP3b, MP3c, and MP3d. It does not seem to intrinsically increase the error of MP2a and MP3a methods. Going to aug-cc-pVDZ has similar, although less severe results, except that MP3b does not seem to be significantly affected.
3. Starting with a large parent grid (e.g. SG-1 or even SG-0⁴¹) and pruning the final grid size via the cutoff parameter ϵ seems to produce superior, balanced grids for a given target grid size.
4. LS-THC methods that involve factorization of the amplitudes incur intrinsic errors that cannot practically be eliminated by increasing the grid size. The errors for MP3b seem to be primarily due to missing angular correlation, which is short-range but still formally non-local.

5. The amplitude factorization in MP2b, MP3c, and MP3d is equivalent to a factorization of the exchange integrals. This incurs a large error as the exchange operator is highly non-local. The same is true for any iterative LS-THC method with an “MP2-like” energy functional (e.g. LS-THC-LCCD and LS-THC-CCSD).
6. LS-THC methods incur a size-consistency error due to the fact that the error for small systems is essentially zero, but linearly increasing above a certain threshold. This error is small, however, and does not increase with system size.
7. Practical crossover for MP3b and MP3d is achieved around 240 correlated electrons. Smaller crossover may be expected with further development.

These conclusions highlight several areas for potential improvement in LS-THC methods, but also indicate that LS-THC-MP3b, at the very least, is promising as a practical method.

ACKNOWLEDGMENTS

This work was supported by a generous start-up grant from SMU and in part by the National Science Foundation (OAC 2003931). All calculations were performed on the Mane-Frame II system at the SMU Center for Scientific Computation.

SUPPLEMENTARY MATERIAL

An electronic supplementary information file is available as zip file (.zip). This file contains the the raw canonical, DF-, and LS-THC-MP n correlation energies, timings, and grid parameters (in Microsoft Excel, .xlsx), as well as molecular geometries (.xyz).

DATA AVAILABILITY

The conclusions in this work are supported by data included in the manuscript and in supporting information files available online.

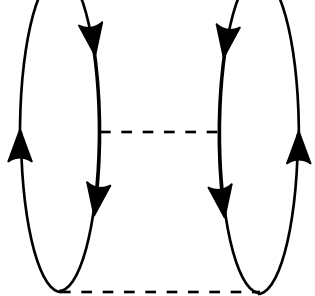
REFERENCES

- ¹W. Kohn. Density Functional and Density Matrix Method Scaling Linearly with the Number of Atoms. *Phys. Rev. Lett.*, 76(17):3168–3171, 1996.
- ²Christof Hättig, David P. Tew, and Benjamin Helmich. Local explicitly correlated second- and third-order Møller–Plesset perturbation theory with pair natural orbitals. *J. Chem. Phys.*, 136(20):204105, 2012.
- ³Christoph Riplinger and Frank Neese. An efficient and near linear scaling pair natural orbital based local coupled cluster method. *J. Chem. Phys.*, 138(3):034106, 2013.
- ⁴Max Schwilk, Qianli Ma, Christoph Köppl, and Hans-Joachim Werner. Scalable Electron Correlation Methods. 3. Efficient and Accurate Parallel Local Coupled Cluster with Pair Natural Orbitals (PNO-LCCSD). *J. Chem. Theory Comput.*, 13(8):3650–3675, 2017.
- ⁵Yang Guo, Christoph Riplinger, Ute Becker, Dimitrios G. Liakos, Yury Minenkov, Luigi Cavallo, and Frank Neese. Communication: An improved linear scaling perturbative triples correction for the domain based local pair-natural orbital based singles and doubles coupled cluster method [DLPNO-CCSD(T)]. *J. Chem. Phys.*, 148(1):011101, 2018.
- ⁶Kazuo Kitaura, Eiji Ikeo, Toshio Asada, Tatsuya Nakano, and Masami Uebayasi. Fragment molecular orbital method: An approximate computational method for large molecules. *Chemical Physics Letters*, 313(3):701–706, 1999.
- ⁷Mark S. Gordon, Mark A. Freitag, Pradipta Bandyopadhyay, Jan H. Jensen, Visvaldas Kairys, and Walter J. Stevens. The Effective Fragment Potential Method: A QM-Based MM Approach to Modeling Environmental Effects in Chemistry. *J. Phys. Chem. A*, 105(2):293–307, 2001.
- ⁸Zoltán Rolik and Mihály Kállay. A general-order local coupled-cluster method based on the cluster-in-molecule approach. *J. Chem. Phys.*, 135(10):104111, 2011.
- ⁹Zoltán Rolik, Lóránt Szegedy, István Ladjánszki, Bence Ladóczki, and Mihály Kállay. An efficient linear-scaling CCSD(T) method based on local natural orbitals. *J. Chem. Phys.*, 139(9):094105, 2013.
- ¹⁰Janus J. Eriksen, Pablo Baudin, Patrick Ettenhuber, Kasper Kristensen, Thomas Kjærgaard, and Poul Jørgensen. Linear-Scaling Coupled Cluster with Perturbative Triple Excitations: The Divide–Expand–Consolidate CCSD(T) Model. *J. Chem. Theory Comput.*, 11(7):2984–2993, 2015.

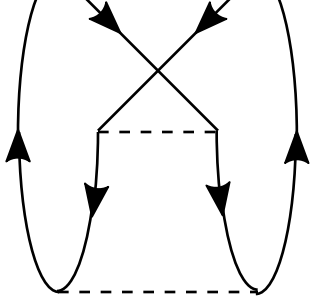
- ¹¹Wei Li, Zhigang Ni, and Shuhua Li. Cluster-in-molecule local correlation method for post-Hartree–Fock calculations of large systems. *Mol. Phys.*, 114(9):1447–1460, 2016.
- ¹²Christian Ochsenfeld, Jörg Kussmann, and Daniel S. Lambrecht. Linear-Scaling Methods in Quantum Chemistry. In *Reviews in Computational Chemistry*, pages 1–82. John Wiley & Sons, Ltd, 2007.
- ¹³Achintya Kumar Dutta, Frank Neese, and Róbert Izsák. Towards a pair natural orbital coupled cluster method for excited states. *J. Chem. Phys.*, 145(3):034102, 2016.
- ¹⁴Achintya Kumar Dutta, Marcel Nooijen, Frank Neese, and Róbert Izsák. Exploring the Accuracy of a Low Scaling Similarity Transformed Equation of Motion Method for Vertical Excitation Energies. *J. Chem. Theory Comput.*, 14(1):72–91, 2018.
- ¹⁵Chong Peng, Marjory C. Clement, and Edward F. Valeev. State-Averaged Pair Natural Orbitals for Excited States: A Route toward Efficient Equation of Motion Coupled-Cluster. *J. Chem. Theory Comput.*, 14(11):5597–5607, 2018.
- ¹⁶Peter Pinski and Frank Neese. Communication: Exact analytical derivatives for the domain-based local pair natural orbital MP2 method (DLPNO-MP2). *J. Chem. Phys.*, 148(3):031101, 2018.
- ¹⁷T. Kolda and B. Bader. Tensor Decompositions and Applications. *SIAM Rev.*, 51(3):455–500, 2009.
- ¹⁸Henk A. L. Kiers. Towards a standardized notation and terminology in multiway analysis. *J. Chemom.*, 14(3):105–122, 2000.
- ¹⁹Udo Benedikt, Alexander A. Auer, Mike Espig, and Wolfgang Hackbusch. Tensor decomposition in post-Hartree–Fock methods. I. Two-electron integrals and MP2. *J. Chem. Phys.*, 134(5):054118, 2011.
- ²⁰Edward G. Hohenstein, Robert M. Parrish, and Todd J. Martínez. Tensor hypercontraction density fitting. I. Quartic scaling second- and third-order Møller-Plesset perturbation theory. *J. Chem. Phys.*, 137(4):044103, 2012.
- ²¹Robert M. Parrish, Edward G. Hohenstein, Todd J. Martínez, and C. David Sherrill. Tensor hypercontraction. II. Least-squares renormalization. *J. Chem. Phys.*, 137(22):224106, 2012.
- ²²Roman Schutski, Jinmo Zhao, Thomas M. Henderson, and Gustavo E. Scuseria. Tensor-structured coupled cluster theory. *J. Chem. Phys.*, 147(18):184113, 2017.

- ²³Felix Hummel, Theodoros Tsatsoulis, and Andreas Grüneis. Low rank factorization of the Coulomb integrals for periodic coupled cluster theory. *J. Chem. Phys.*, 146(12):124105, 2017.
- ²⁴Sara I. L. Kokkila Schumacher, Edward G. Hohenstein, Robert M. Parrish, Lee-Ping Wang, and Todd J. Martínez. Tensor Hypercontraction Second-Order Møller–Plesset Perturbation Theory: Grid Optimization and Reaction Energies. *J. Chem. Theory Comput.*, 11(7):3042–3052, 2015.
- ²⁵Udo Benedikt, Karl-Heinz Böhm, and Alexander A. Auer. Tensor decomposition in post-Hartree–Fock methods. II. CCD implementation. *J. Chem. Phys.*, 139(22):224101, 2013.
- ²⁶Robert M. Parrish, Yao Zhao, Edward G. Hohenstein, and Todd J. Martínez. Rank reduced coupled cluster theory. I. Ground state energies and wavefunctions. *J. Chem. Phys.*, 150(16):164118, 2019.
- ²⁷Edward G. Hohenstein, Robert M. Parrish, C. David Sherrill, and Todd J. Martínez. Communication: Tensor hypercontraction. III. Least-squares tensor hypercontraction for the determination of correlated wavefunctions. *J. Chem. Phys.*, 137(22):221101, 2012.
- ²⁸Danylo Kats, Denis Usvyat, and Martin Schütz. On the use of the Laplace transform in local correlation methods. *Phys. Chem. Chem. Phys.*, 10(23):3430–3439, 2008.
- ²⁹A. D. Becke. A multicenter numerical integration scheme for polyatomic molecules. *J. Chem. Phys.*, 88(4):2547–2553, 1988.
- ³⁰Devin A. Matthews. Improved Grid Optimization and Fitting in Least Squares Tensor Hypercontraction. *J. Chem. Theory Comput.*, 16(3):1382–1385, 2020.
- ³¹Francesco Aquilante, Roland Lindh, and Thomas Bondo Pedersen. Unbiased auxiliary basis sets for accurate two-electron integral approximations. *J. Chem. Phys.*, 127(11):114107, 2007.
- ³²Rick A. Kendall and Herbert A. Früchtl. The impact of the resolution of the identity approximate integral method on modern ab initio algorithm development. *Theor Chem Acta*, 97(1):158–163, 1997.
- ³³Henrik Koch, Alfredo Sánchez de Merás, and Thomas Bondo Pedersen. Reduced scaling in electronic structure calculations using Cholesky decompositions. *J. Chem. Phys.*, 118(21):9481–9484, 2003.
- ³⁴Francesco Aquilante, Thomas Bondo Pedersen, and Roland Lindh. Low-cost evaluation of the exchange Fock matrix from Cholesky and density fitting representations of the electron

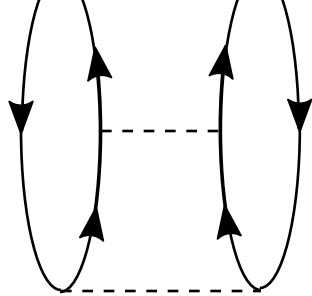
- repulsion integrals. *J. Chem. Phys.*, 126(19):194106, 2007.
- ³⁵Joonho Lee, Lin Lin, and Martin Head-Gordon. Systematically Improvable Tensor Hypercontraction: Interpolative Separable Density-Fitting for Molecules Applied to Exact Exchange, Second- and Third-Order Møller–Plesset Perturbation Theory. *J. Chem. Theory Comput.*, 16(1):243–263, 2020.
- ³⁶S. Koch and W. Kutzelnigg. Comparison of CEPA and CP-MET methods. *Theoret. Chim. Acta*, 59(4):387–411, 1980.
- ³⁷Thom H. Dunning. Gaussian basis sets for use in correlated molecular calculations. I. The atoms boron through neon and hydrogen. *J. Chem. Phys.*, 90(2):1007–1023, 1989.
- ³⁸Florian Weigend, Andreas Köhn, and Christof Hättig. Efficient use of the correlation consistent basis sets in resolution of the identity MP2 calculations. *J. Chem. Phys.*, 116(8):3175–3183, 2002.
- ³⁹Peter M. W Gill, Benny G Johnson, and John A Pople. A standard grid for density functional calculations. *Chemical Physics Letters*, 209(5):506–512, 1993.
- ⁴⁰Devin A. Matthews, Lan Cheng, Michael E. Harding, Filippo Lipparini, Stella Stopkowicz, Thomas-C. Jagau, Péter G. Szalay, Jürgen Gauss, and John F. Stanton. Coupled-cluster techniques for computational chemistry: The CFOUR program package. *J. Chem. Phys.*, 152(21):214108, 2020.
- ⁴¹Siu-Hung Chien and Peter M. W. Gill. SG-0: A small standard grid for DFT quadrature on large systems. *J. Comput. Chem.*, 27(6):730–739, 2006.



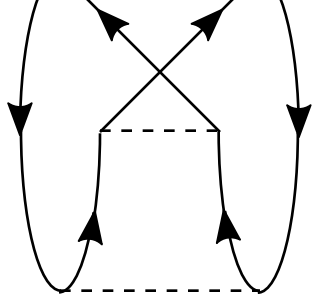
E_{PPC}



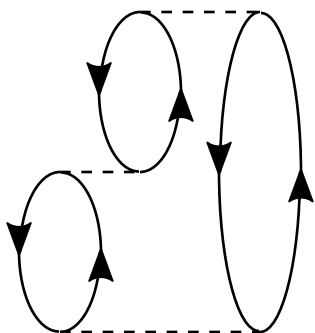
E_{PPX}



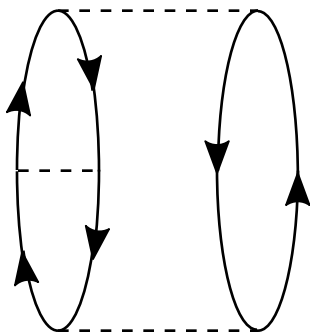
E_{HHC}



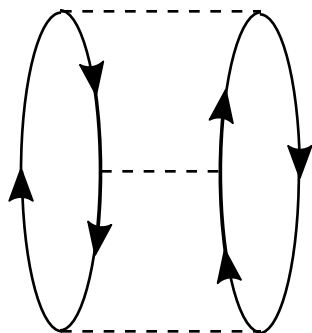
E_{HHX}



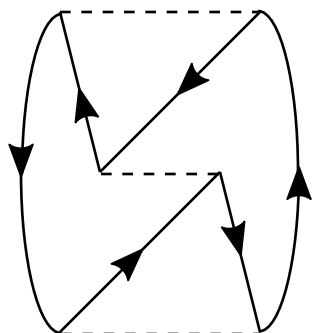
E_{PH1}



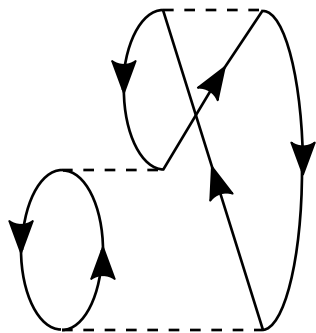
E_{PH2}



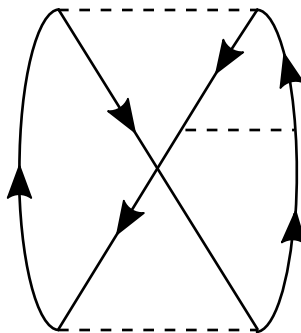
E_{PH3}



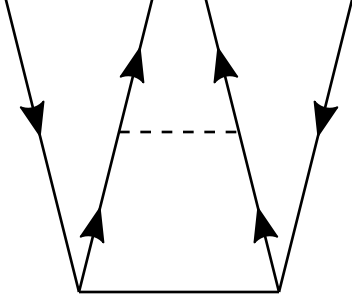
E_{PH4}



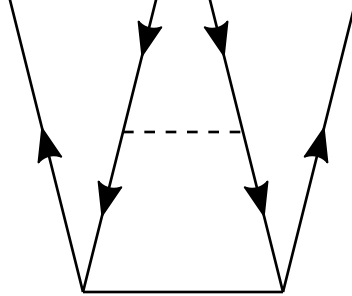
$E_{\text{PH5}}(\text{x2})$



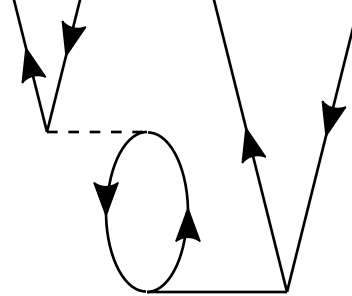
$E_{\text{PH6}}(\text{x2})$



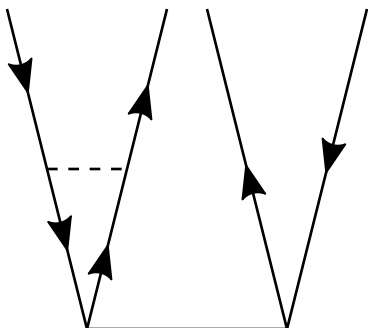
PP



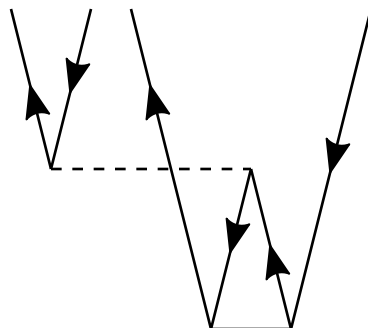
HH



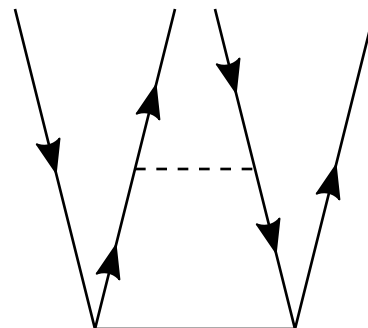
PH1



PH2



PH3



PH4